Experimental Measurement of Negative Grain-Boundary Triple Line Tension

Xiuming Xiao and Ziren Wang*
Department of Physics, Chongqing University, Chongqing 401331, China

(Received 21 July 2025; accepted 15 January 2026; published 9 February 2026)

We measured negative grain-boundary triple line tension within bulk hard-sphere colloidal polycrystals. Compared to the grain boundaries, the tension is predominantly distributed in the grain lattices. The negative tension drives finite premelting at triple junctions and leads to a marginally denser lattice nearby.

DOI: 10.1103/t23n-bch4

A triple line appears when three phases or grain boundaries (GBs) meet. During the 1870s, Gibbs [1] postulated the existence of line tension arising from excess free energy at the confluence of fluid boundaries. To date, however, the interpretation, magnitude, and even the sign of the line tension are still highly debated, although experiments have demonstrated the important roles that triple lines play in various material behaviors. For triple junctions presented by three GBs, computer simulations show the triple lines can exhibit either positive [2–6] or negative [7–9] tension. In contrast, experimental studies report only positive values [10–15]. The previous experiments were conducted at the triple junction pits on the free surface of polycrystals, and each pit is essentially a quadruple point joined by four triple junctions. For this case, the tension of the four lines and the free energy of the quadruple point must be considered together, which makes the experimental measurements somewhat lacking in an accurate thermodynamic description. Colloids serve as atomic model systems, offering exceptional real-space imaging in the interior of crystals at single-particle dynamics [16,17], which allows us to follow the Gibbsian construction regarding the triple line tension. Consequently, in this Letter, we measured the tension for single triple lines through direct observation of premelting at triple junctions within bulk hard-sphere colloidal polycrystals by video microscopy. We found that the triple line tension is negative.

We synthesized the *N*-isopropylacrylamide microgel colloids by the method described in Ref. [18]. The measured pair interaction (Fig. S1 [19]) is short-range repulsive, which is close to hard spheres. We prepared the sample by loading the colloidal suspension into a glass channel ($18.0 \times 3.0 \times 0.2$ mm^3) and annealed it into face-centered cubic (fcc) polycrystals. In each domain, the (111) face is parallel to the imaging plane. After several days of equilibration, each GB and triple line should have reached a stable configuration. We analyzed triple junctions consisting of $\langle 111 \rangle$ tilt GBs, ensuring all triple lines are normal to the imaging plane. GBs connecting the nearest triple junctions are typically greater than 400 particle diameters. At such a length, the grain size should have a minor effect on the triple line tension, and the triple junctions can be regarded as separated. The excellent refractive-index matching between particles and water enables us to see through all ~150 layers using the transmission mode of a bright-field microscope. Images for measurements were acquired around the middle of the sample layers. The thermoresponsive colloids exhibit a linear diameter σ variation from 1.56 μm at reading temperature 28.80 °C to 1.50 μm at 31.60 °C (Fig. S2 [19]). The ambient temperature T_{ambient} is controlled through circulating water baths to uniformly heat a sample area of ~20 mm^2 at a step of 0.05 °C. By tuning the temperature, we could change the volume fraction ϕ to melt the sample. Notably, ϕ is the governing parameter for the phase behaviors of hard-sphere systems. In addition to the uniform heating, we could focus a beam of light emitted from a mercury lamp by the objective through the reflection mode to locally heat a $4\pi/3(100\ \mu\text{m})^2$ (field of view) by 60 μm region in the interior of the polycrystals, which gives rise to a temperature increase δT up to 2.50 °C (5.5% change of ϕ) over T_{ambient} in the chosen region. The local heating technique was initially developed to investigate the homogeneous melting of crystals [17,39]. Here, we adopted this technique to measure the referential GB energy [Fig. 2]. By analyzing the Lindemann parameter (Fig. S3 [19]), the bulk melting temperature $T_{\text{m}} = 29.40$ °C is precisely located, corresponding to the melting volume fraction $\phi_{\text{m}} = 54.5\%$. When heating the sample, triple junctions premelt to a discernible size around $T_{\text{m}} - 0.50$ °C (i.e., $\phi = 55.6\%$). By contrast, all GBs keep their original structures until T_{m}. It has been demonstrated that $\langle 111 \rangle$ tilt GBs can stay superheated for hard-sphere systems [20], in which case the degree of superheating $\Delta T \equiv T_{\text{ambient}} + \delta T - T_{\text{m}} > 0$.

*Contact author: wziren@cqu.edu.cn

Published by the American Physical Society under the terms of the Creative Commons Attribution 4.0 International license. Further distribution of this work must maintain attribution to the author(s) and the published article's title, journal citation, and DOI.

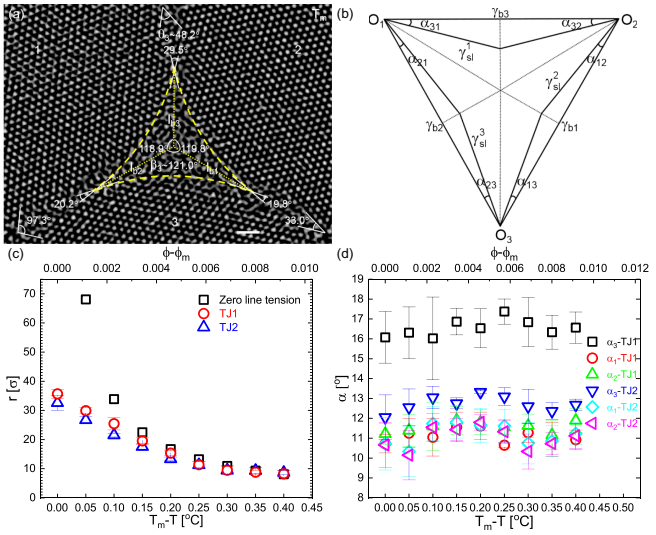


FIG. 1. (a) Real-space cross-sectional image of the triple junction TJ1 at T_m. All lines represent a section perpendicular to the surface. (b) Schematic diagram indicating the relation between dihedral angles and interfacial energies. (c), (d) Equilibrium radius of curvature of the solid-liquid interface r and dihedral angle α, respectively, at each temperature for triple junctions TJ1 and TJ2. The square symbols in (c) denote the case under zero line tension. Error bars stand for the standard error. Scale bar: 5 μm.

The area of the premelted liquid pocket S [Fig. 3(b)] that is bounded by three cylindrical solid-liquid interfaces (curvilinear lines in Figs. 1(a) and S5 [19]) increases continuously with temperature (Supplemental Material [19], Movie 1). The liquid pocket is uniform along the entire triple line, extending from the cover glass to the glass slide, and is too small to affect ϕ. Due to heat dissipation, the sample temperature rises less than 0.20 °C during the premelting, keeping the system nearly isothermal. More details on experimental systems and identifying the solid-liquid interfaces are provided in Supplemental Material [19].

Next, we calculated the triple line tension through measurements on the premelting at triple junctions. Throughout the premelting volume fraction variations, the triple line tension, as well as the GB energy γ_b and the solid-liquid interfacial energy γ_{sl}, should remain almost constant, as warranted by the Gibbs isotherm. We assumed that the solid structures would not be changed significantly by the presence of the molten liquids. In general, the rigidity of solids is so great that any tendency of solid-liquid interfaces to vary in area or form may be neglected in comparison with the forces that are produced in the interior of the solids by any sensible strains. $F - \sum \mu_i N_i$ is the natural free energy function to characterize the system studied, where F is the Helmholtz function, μ_i is the chemical potential, and N_i is the total number of the individual chemical components. The tension κ for a supposed line is defined as the free energy change upon forming a single triple junction, which can be expressed as

$$\kappa = \int_D (p^{\mathrm{ref}} - p(\mathbf{r}))\mathrm{d}\mathbf{r} + \sum_k \int_S (\gamma_{bk}(\mathbf{r}) - \gamma_{\mathrm{ref}}^k)\mathrm{d}\mathbf{r}, \quad (1)$$

where p^{ref} and γ_{ref} denote the referential pressure and referential GB energy far from the triple line, respectively. The first and the second terms of Eq. (1) respectively constitute the contributions of bulk grain lattices and local GB planes to the triple line tension. Some derivation is required to make Eq. (1) experimentally measurable. The triple line follows the force balance that $\gamma_{b1}/\sin\beta_1 = \gamma_{b2}/\sin\beta_2 = \gamma_{b3}/\sin\beta_3$, where β is the dihedral angle between GBs [Fig. 1(a)]. This relationship can be verified by measuring β and α [Fig. 1(d)]. Basically, a triple line satisfies the Herring equation [40], where additional torque terms defined as the derivative of γ_b with respect to the inclination angles, together with γ_b, describe the mechanical equilibrium. However, all studied GBs [Figs. 1(a) and S5 [19]] are asymmetric and off the high-coincidence orientations. Thus, the torque terms contribute little, if any, to the total capillary vector [41]. Based on the balance, we form a triangle $O_1O_2O_3$ having sides equal to γ_{bk} and suppose the sides to be perpendicular to the GBs [Fig. 1(b)]. Upon O_1O_2, we may then construct a sub triangle having sides equal to γ_{b3}, γ_{sl}^1, and γ_{sl}^2, where γ_{sl}^i represents the interfacial energy between liquids and grain i. Similar operations apply to O_2O_3 and O_3O_1. Then the geometry obeys the Young's equation $\gamma_{bk} = \gamma_{sl}^i \cos\alpha_{ki} + \gamma_{sl}^j \cos\alpha_{kj}$, where α denotes the dihedral angle. Specifically, the six interfacial energies give the total curvatures in degrees of the three solid-liquid interfaces, and the pressures will give the radii of these curvatures. Given identical grains and weak anisotropy of γ_{sl} for hard-sphere systems [42], the three interfaces should share a radius of curvature r (hence $\gamma_{bk} = 2\gamma_{sl}\cos\alpha_k$), as confirmed by our uniform curvature fits in Figs. 1(a) and S5 [19]. The measured r monotonically increases as temperature rises [Fig. 1(c)]. r was chosen to be positive when the interfaces are convex toward the liquids. All measured αs [Fig. 1(d)] vary little during the premelting and are nonzero because GBs can be superheated.

At each equilibrium state, $\mu_s(p) = \mu_l(p_l)$, where $p_l = p - \gamma_{sl}/r$ is the pressure of the premelted liquids. μ_s and μ_l represent the chemical potentials of solids and liquids, respectively. There should be another pressure of liquids p_l^{ref} that fits $\mu_s(p^{\mathrm{ref}}) = \mu_l(p_l^{\mathrm{ref}})$. If we expand $\mu_s(p^{\mathrm{ref}})$ and $\mu_l(p_l^{\mathrm{ref}})$ near the melting point with only linear term retained, then we have $(p^{\mathrm{ref}} - p_{co})(v_f - v_m) = (p^{\mathrm{ref}} - p_l^{\mathrm{ref}})v_f$. p_{co} is the coexistence pressure. $v_{f,m} = \pi\sigma^3/6\phi_{f,m}$ is the volume per particle of the liquid/solid phase at coexistence. A similar formalism also exists between p and p_l. The term on the left side can be approximated by the chemical potential difference $\Delta\mu = \mu_l - \mu_s$ at p^{ref}, thus $p^{\mathrm{ref}} - p_l^{\mathrm{ref}} = \Delta\mu/v_f$. Meanwhile, it is straightforward to verify that $p^{\mathrm{ref}} - p_l^{\mathrm{ref}} + p_l - p = (1 - v_m/v_f)(p^{\mathrm{ref}} - p)$. Therefore, we obtained

$p^{\mathrm{ref}} - p = (\Delta\mu - \gamma_{\mathrm{sl}} v_{\mathrm{f}}/r)/(v_{\mathrm{f}} - v_{\mathrm{m}})$. Referring to our earlier experimental estimate [20], $\gamma_{\mathrm{sl}} = 0.58\ k_{\mathrm{B}}T/\sigma^2$, in line with simulations [42–44] for hard-sphere systems. $\Delta\mu$ [Fig. 3(a)] is exactly computable from equations of state (see Supplemental Material [19]).

As to the second term on the right side of Eq. (1), γ_{ref} is measured upon the contact angle φ of the critical nucleus [Fig. 2] far away from the triple line ($\sim 200\,\sigma$). According to the classical nucleation theory [20,45], superheated GBs undergo heterogeneous nucleation melting, by which subcritical nuclei form and disappear until one reaches the critical size. The critical nucleus is confirmed by adjusting T_{ambient} by ± 0.05°C such that the liquid nucleus has an equal probability of growing or shrinking (see Supplemental Material [19]). The nucleus presents symmetrical, abutted spherical caps on either side of the GB face, as indicated by our three-dimensional (3D) scan. Figure 2(a) (Supplemental Material [19], Movie 2) shows a real image of the largest cross-section of a critical nucleus. Interfacial balance yields $\gamma_{\mathrm{ref}}^{k} = 2\gamma_{\mathrm{sl}} \cos\varphi_k$, in which φ_k is measured by $\cos^{-1}[(a^2 - b^2)/(a^2 + b^2)]$.

Given the above, we rewrote Eq. (1) as

$$\kappa/\sigma = \int \frac{1}{v_{\mathrm{f}} - v_{\mathrm{m}}} \left(\Delta\mu - \frac{\gamma_{\mathrm{sl}}}{r} v_{\mathrm{f}}\right) \mathrm{d}S + 2\gamma_{\mathrm{sl}} \sum \int (\cos\alpha_k - \cos\varphi_k)\,\mathrm{d}l_{bk}, \qquad (2)$$

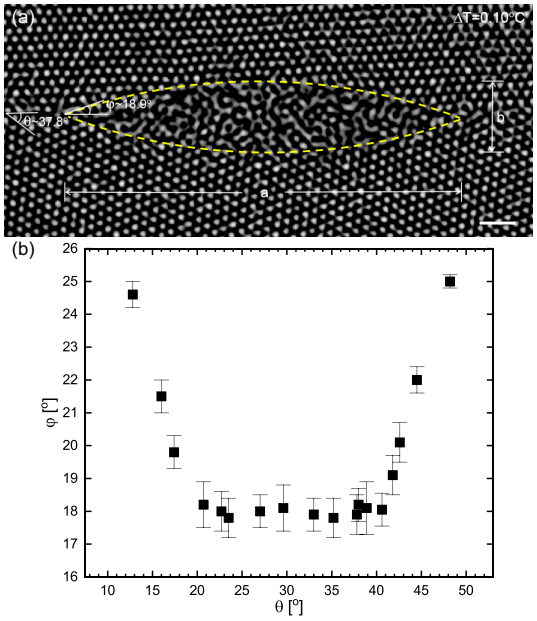


FIG. 2. (a) Largest cross-sectional real image for the critical nucleus through heterogeneous nucleation on a GB at $\Delta T = 0.10$ °C, corresponding to GB2 of TJ2 (Fig. S5 [19]). (b) Contact angle φ as a function of misorientation angle θ, statistics for different inclinations. Error bars stand for the standard error. Scale bar: 5 μm.

where l_{bk} [Fig. 3(c)] is the length of each molten GB (dotted lines in Figs. 1(a) and S5 [19]). We examined two triple-junction configurations categorized by distinct combinations of γ_{ref}. As Fig. 2(b) shows, γ_{ref} increases with GB misorientation θ and saturates when $\theta \gtrsim 19°$, corresponding to the transition to a high-angle GB. When $\theta \lesssim 12°$, a GB exhibits an array of dislocations, making either the premelting at triple junctions or the nucleation on GBs a discontinuous process. Accordingly, the first configuration consists of two high-angle GBs, labeled as TJ1 [Fig. 1(a)], with tilt angles (open towards the triple junction) of 33.0°, 97.3°, and 48.2°. The other configuration, labeled as TJ2 (Fig. S5 [19]), features three high-angle GBs with tilt angles of 20.7°, 82.2°, and 77.4°. As plotted in Fig. 3(d), for both configurations, we found the line tension is negative (solid symbols) and resides almost in the bulk lattices. Specifically, the negative contribution of grain lattices, ninefold greater in magnitude than the GBs' positive contribution, results in net negative line tension. Since all measured rs are smaller than that for zero line tension [Fig. 1(c)], the line tension monotonically gets negative with S, and finally weakens the original GB energy by ~30% if only the premelted region is considered [Fig. 3(d)]. This reduction ratio is comparable to that reported for simulations of pure fcc metals at small grain sizes [7]. The negative line tension agrees with the density diagram, as shown in Fig. 4, where each solid particle is colored by its instantaneous local volume fraction. We found that the region near the triple junction exhibits a marginally higher density, which reduces the amplitude of particles' thermal vibrations and consequently yields a more ordered

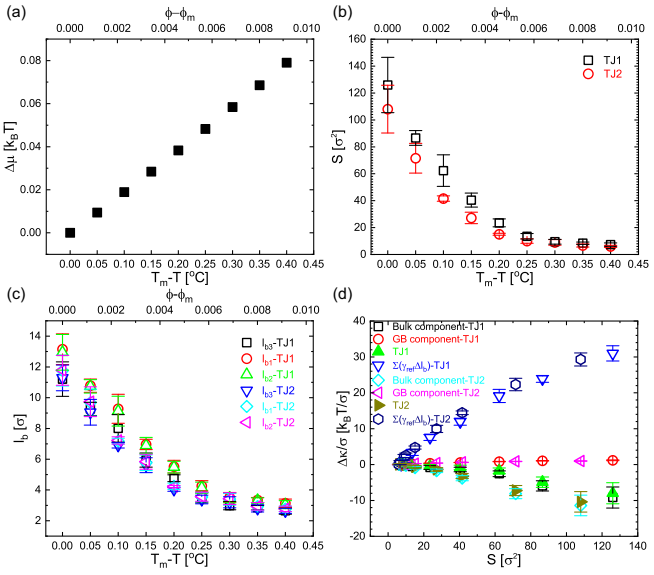


FIG. 3. (a)–(c) Chemical potential difference $\Delta\mu$, area of the liquid pocket S, and length of the molten GB l_{b} as a function of temperature. Error bars stand for the standard error. (d) Change in the line tension and its constituent components as a function of S, given by the Riemann sum of Eq. (2). Error bars stand for the uncertainty in indirect measurements.

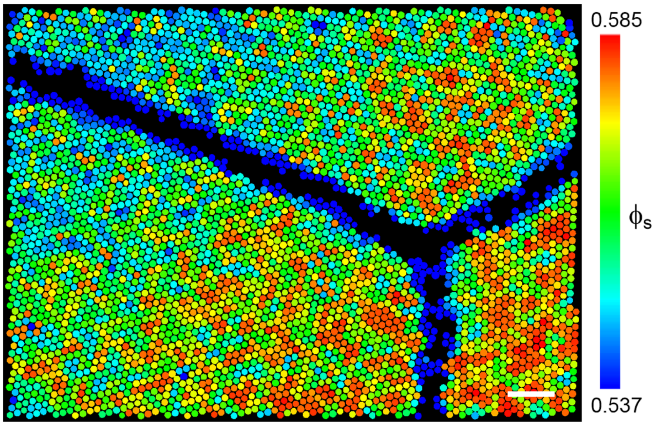


FIG. 4. Fake-colored microscopy image of triple junction TJ1 at $T_m - 0.70\,°C$ (i.e., $\phi = 56.1\%$), where each solid particle is colored according to its instantaneous local volume fraction ϕ_s calculated from the two-dimensional Voronoi cell. The rest of the particles are colored black. The region near the triple junction exhibits a slightly larger packing fraction than the others. Scale bar: 10 μm.

lattice structure in real-space observations. This trend is evident as it moves away from the triple junction on a sufficiently large scale ($\gtrsim 60\,\sigma$). Importantly, such density nonuniformity, which persists at temperatures as low as $T_m - 1.40\,°C$ (i.e., $\phi = 57.7\%$), implies lower local potential near the triple junction and qualitatively indicates negative line tension. This potential reduction might stem from variations in specific fields arising from the constituent GBs when they approach each other, among other possible factors. Like standard line defects, the triple line tension is delocalized and has a long-range effect, as proposed before [46]. Each GB energy increases slightly as it approaches the triple junction [Fig. 3(d)], consistent with the argument [4] that individual GBs do not generally correspond to energy minima at a triple junction because of mutual interactions. The triple junction TJ1, comprising one low-angle GB, appears to have less negative line tension than TJ2.

We try to write κ explicitly as a function of r. Theoretically, based on Figs. 1(a) and 1(b), S can be written as $r^2 F_S$, where $F_S = f + \sum \alpha_k - 1/2(\sum \sin 2\alpha_k + \pi)$ is a geometry factor in terms of α, and $f = ((\sum \cos^2 \alpha_k)^2 - 2\sum \cos^4 \alpha_k)^{1/2}$. Similarly, $l_{bk} = rF_{bk}$, where $F_{bk} = \cos\alpha_k(\cos^2\alpha_i + \cos^2\alpha_j - \cos^2\alpha_k)/f - \sin\alpha_k$. In our case, F_S and F_{bk} can be regarded as constant. Furthermore, the general condition of mechanical equilibrium requires that $2(\sum F_{bk}\cos\alpha_k - F_S) = F_{sl}$, where $F_{sl} = \pi - 2\sum \alpha_k$ is the corresponding factor that quantifies the total solid-liquid interface length. Consequently, during the premelting, Eq. (2) reduces to

$$\kappa(r)/\sigma = \int \left(\frac{2F_S}{v_f - v_m}(r\Delta\mu - v_m\gamma_{sl}) + (F_{sl} - 2\sum F_{bk}\cos\varphi_k)\gamma_{sl} \right) dr. \quad (3)$$

The line tension given by Eq. (3) (Fig. S6 [19]) differs from that of Eq. (2) by ~5%. The analytical form $\kappa(r)$ can serve as a corrective term for the free energy change in the study of premelting at triple junctions, in some aspects resembling the disjoining potential [47,48] that was introduced to interpret different premelting behaviors of GBs. However, their physical nature is different. We note that regardless of the presence of GB premelting, premelting at triple junctions always occurs first and is more extensive [20,21].

The line tension should equal the integral of S from zero to infinity. However, we are not able to measure a larger S because once the temperature is above T_m, uniform liquid layers rapidly spread along GBs, establishing interconnections between triple junctions [20]. One might expect that $d\kappa/dS|_{S\to\infty} = 0$. With regard to a smaller S, it must be a peculiar state of equilibrium in which both measurements and theoretical models cease to be accurate. Although we only measured the change in the line tension, the trend is clear to judge the sign. In fact, the negative line tension can be inferred directly from the shape of the liquid pocket at T_m [Fig. 1(a)]. Supposing that in the absence of κ, a positive r implies insufficient solid-liquid interfacial energy compensation for GB energy loss (i.e., $\sum F_{bk}\gamma_{bk} > F_{sl}\gamma_{sl}$). Subject to a constant ϕ, any small increase in S will lead to a decrease in the free energy unless negative line tension intervenes. Therefore, the negative line tension plays a decisive role in the finite premelting of triple junctions. This reasoning suggests negative line tension in aluminum, based on transmission electron microscopy observations [21] of this finite premelting at T_m with $r > 0$. Possible signs of the line tension in various systems are discussed in Supplemental Material [19].

Here are some points worth mentioning. First, in general, the pressure p in Eq. (1) should be expressed in terms of the stress tensor. Nevertheless, the high mobility of particles as the system approaches T_m justifies the use of classical capillarity theory, thereby ensuring the validity of the derived free energy and related conclusions. In our measurements, the pressure contours are approximated by the solid-liquid interfaces under the assumption of continuity. Second, the line tension measured does not include the contribution from the core energy. Also, we did not rule out the effect of the solid-solid-liquid triple line tension and the effect of the possible GB disjoining potential [47,48] in relevant derivations. Thus, the line tension has already been a result of taking both factors into account. Regarding the triple lines that arise at the glass walls, we found that they have a minor effect, as both the local heating and the uniform heating methods yield nearly the same GB triple line tension. Third, King [49] has emphasized the rationale for the existence of negative GB triple line tension, countering the argument that negative line tension would result in a spontaneous multiplication of triple junctions. Fourth, Gibbs took two adhered soap bubbles as an example to infer the existence of negative triple line tension [1]. However, the

interface there consists of a thin film of liquid between two liquid-vapor surfaces, not a so-called interface [50–52]. Fifth, we did not observe the GBs become apparently roughened below T_m (Supplemental Material [19], Movie 1), consistent with previous experimental observation for 3D hard-sphere colloidal polycrystals [22]. At last, the curvature effect on γ_{sl} is negligible since even the minimum r [Fig. 1(c)] is larger than 5σ [53,54].

As a fundamental structure of poly- and nanocrystals, triple junctions have been overlooked compared to GBs or surfaces [46,55,56]. Previous studies have revealed that triple junctions exhibit a more substantial impact than GBs on phase transformation [20,21], segregation [57,58], intergranular diffusion [59,60], and grain growth during the coarsening [61,62]. Triple line tension studies provide a robust framework for interpreting these distinct behaviors. Although some schemes [46,52,63] have been proposed, convincing measurements of the triple line tension remain elusive due to persistent experimental challenges. Here, under the Gibbsian construction, we measured negative thermodynamic triple line tension within bulk hard-sphere colloidal polycrystals.

Acknowledgments—This work is supported by the National Natural Science Foundation of China (Grant No. 12074047).

Data availability—The data that support the findings of this Letter are openly available [64].

[1] J. W. Gibbs, On the equilibrium of heterogeneous substances, Trans. Conn. Acad. Arts Sci. **3**, 343 (1877–1878), https://www.biodiversitylibrary.org/item/32295.
[2] S. Costantini, P. Alippi, L. Colombo, and F. Cleri, Triple junctions and elastic stability of polycrystalline silicon, Phys. Rev. B **63**, 045302 (2000).
[3] A. Caro and H. Van Swygenhoven, Grain boundary and triple junction enthalpies in nanocrystalline metals, Phys. Rev. B **63**, 134101 (2001).
[4] S. Shekhar and A. H. King, Strain fields and energies of grain boundary triple junctions, Acta Mater. **56**, 5728 (2008).
[5] A. A. Nazarov, D. V. Bachurin, O. A. Shenderova, and D. W. Brenner, On the origin and energy of triple junction defects due to the finite length of grain boundaries, Interface Sci. **11**, 417 (2003).
[6] I. Adlakha and K. N. Solanki, Structural stability and energetics of grain boundary triple junctions in face centered cubic materials, Sci. Rep. **5**, 8692 (2015).
[7] N. Tuchinda and C. A. Schuh, Triple junction excess energy in polycrystalline metals, Acta Mater. **279**, 120274 (2024).
[8] S. G. Srinivasan, J. W. Cahn, H. Jónsson, and G. Kalonji, Excess energy of grain-boundary trijunctions: An atomistic simulation study, Acta Mater. **47**, 2821 (1999).
[9] S. M. Eich and G. Schmitz, Embedded-atom study of low-energy equilibrium triple junction structures and energies, Acta Mater. **109**, 364 (2016).
[10] D. McLean, *Grain Boundaries in Metals* (Clarendon Press, Oxford, 1957), p. 49.
[11] P. Fortier, G. Palumbo, G. D. Bruce, W. A. Miller, and K. T. Aust, Triple line energy determination by scanning tunneling microscopy, Scr. Metall. Mater. **25**, 177 (1991).
[12] H. Kim, Y. Xuan, P. D. Ye, R. Narayanan, and A. H. King, Anomalous triple junction surface pits in nanocrystalline zirconia thin films and their relationship to triple junction energy, Acta Mater. **57**, 3662 (2009).
[13] B. Zhao, J. C. Verhasselt, L. S. Shvindlerman, and G. Gottstein, Measurement of grain boundary triple line energy in copper, Acta Mater. **58**, 5646 (2010).
[14] H. Rösner, C. Kübel, Y. Ivanisenko, L. Kurmanaeva, S. V. Divinski, M. Peterlechner, and G. Wilde, Strain mapping of a triple junction in nanocrystalline Pd, Acta Mater. **59**, 7380 (2011).
[15] H. Zschiesche, A. Charai, C. Alfonso, and D. Mangelinck, Methods for Gibbs triple junction excess determination: Ti segregation in $CoSi_2$ thin film, J. Mater. Sci. **55**, 13177 (2020).
[16] A. M. Alsayed, M. F. Islam, J. Zhang, P. J. Collings, and A. G. Yodh, Premelting at defects within bulk colloidal crystals, Science **309**, 1207 (2005).
[17] Z. Wang, F. Wang, Y. Peng, Z. Zheng, and Y. Han, Imaging the homogeneous nucleation during the melting of superheated colloidal crystals, Science **338**, 87 (2012).
[18] A. Fernandez-Nieves, H. Wyss, J. Mattsson, and D. A. Weitz, *Microgel Suspensions: Fundamentals and Applications* (John Wiley & Sons, New York, 2011) p. 229.
[19] See Supplemental Material at http://link.aps.org/supplemental/10.1103/t23n-bch4 for additional information on the experimental system, experimental methods, data analysis, calculation of chemical potentials, and captions of the supplementary movies, which includes Refs. [7,16,17,20–38].
[20] X. Xiao, L. Wang, Z. Wang, and Z. Wang, Superheating of grain boundaries within bulk colloidal crystals, Nat. Commun. **13**, 1599 (2022).
[21] T. E. Hsieh and R. W. Balluffi, Experimental study of grain boundary melting in aluminum, Acta Metall. **37**, 1637 (1989).
[22] M. Liao, X. Xiao, S. T. Chui, and Y. Han, Grain-boundary roughening in colloidal crystals, Phys. Rev. X **8**, 021045 (2018).
[23] D. A. Kofke and P. G. Bolhuis, Freezing of polydisperse hard spheres, Phys. Rev. E **59**, 618 (1999).
[24] P. N. Pusey and W. Van Megen, Phase behaviour of concentrated suspensions of nearly hard colloidal spheres, Nature (London) **320**, 340 (1986).
[25] B. Li, X. Xiao, S. Wang, W. Wen, and Z. Wang, Real-space mapping of the two-dimensional phase diagrams in attractive colloidal systems, Phys. Rev. X **9**, 031032 (2019).
[26] B. I. Halperin and D. R. Nelson, Theory of two-dimensional melting, Phys. Rev. Lett. **41**, 121 (1978).
[27] J. Hernández-Guzmán and E. R. Weeks, The equilibrium intrinsic crystal-liquid interface of colloids, Proc. Natl. Acad. Sci. U.S.A. **106**, 15198 (2009).
[28] V. D. Nguyen, M. T. Dang, B. Weber, Z. Hu, and P. Schall, Visualizing the structural solid-liquid transition at colloidal crystal/fluid interfaces, Adv. Mater. **23**, 2716 (2011).

[29] S. H. Behrens and D. G. Grier, Pair interaction of charged colloidal spheres near a charged wall, Phys. Rev. E **64**, 050401(R) (2001).
[30] J. Baumgartl and C. Bechinger, On the limits of digital video microscopy, Europhys. Lett. **71**, 487 (2005).
[31] M. Polin, D. G. Grier, and Y. Han, Colloidal electrostatic interactions near a conducting surface, Phys. Rev. E **76**, 041406 (2007).
[32] F. A. Lindemann, The calculation of molecular vibration frequency, Z. Phys. **11**, 609 (1910).
[33] J. Kolafa, S. Labík, and A. Malijevský, Accurate equation of state of the hard sphere fluid in stable and metastable regions, Phys. Chem. Chem. Phys. **6**, 2335 (2004).
[34] M. N. Bannerman, L. Lue, and L. V. Woodcock, Thermodynamic pressures for hard spheres and closed-virial equation-of-state, J. Chem. Phys. **132**, 084507 (2010).
[35] F. Weinberg and E. Teghtsoonian, Grain-boundary melting, Acta Metall. **5**, 455 (1957).
[36] F. Weinberg, Further observations on grain boundary melting, Acta Metall. **6**, 535 (1958).
[37] R. W. Balluffi and R. Maurer, On rotating sphere-on-a-plate experiments and the questions of whether high angle grain boundaries melt below bulk melting temperatures, Scr. Metall. **22**, 709 (1988).
[38] F. Caupin, S. Sasaki, and S. Balibar, Absence of grain boundary melting in solid helium, J. Phys. Condens. Matter **20**, 494228 (2008).
[39] Z. Wang, F. Wang, Y. Peng, and Y. Han, Direct observation of liquid nucleus growth in homogeneous melting of colloidal crystals, Nat. Commun. **6**, 6942 (2015).
[40] C. Herring, *The Physics of Powder Metallurgy* (McGraw Hill, New York, 1951), p. 143.
[41] D. W. Hoffman and J. W. Cahn, A vector thermodynamics for anisotropic surfaces: I. Fundamentals and application to plane surface junctions, Surf. Sci. **31**, 368 (1972).
[42] A. Härtel, M. Oettel, R. E. Rozas, S. U. Egelhaaf, J. Horbach, and H. Löwen, Tension and stiffness of the hard sphere crystal-fluid interface, Phys. Rev. Lett. **108**, 226101 (2012).
[43] R. L. Davidchack, Hard spheres revisited: Accurate calculation of the solid-liquid interfacial free energy, J. Chem. Phys. **133**, 234701 (2010).
[44] M. Bültmann and T. Schilling, Computation of the solid-liquid interfacial free energy in hard spheres by means of thermodynamic integration, Phys. Rev. E **102**, 042123 (2020).
[45] D. A. Porter, K. E. Easterling, and M. Y. Sherif, *Phase Transformations in Metals and Alloys* (CRC Press, Boca Raton, Florida, 2009).
[46] A. H. King, Triple junction energy and prospects for measuring it, Mater. Sci. Technol. **23**, 505 (2007).
[47] R. Kikuchi and J. W. Cahn, Grain-boundary melting transition in a two-dimensional lattice-gas model, Phys. Rev. B **21**, 1893 (1980).
[48] R. Lipowsky and M. E. Fisher, Scaling regimes and functional renormalization for wetting transitions, Phys. Rev. B **36**, 2126 (1987).
[49] A. H. King, The geometric and thermodynamic properties of grain boundary junctions, Interface Sci. **7**, 251 (1999).
[50] F. Morgan and J. E. Taylor, Destabilization of the tetrahedral point junction by positive triple junction line energy, Scr. Metall. Mater. **25**, 1907 (1991).
[51] J. E. Taylor, Mathematical models of triple junctions, Interface Sci. **7**, 243 (1999).
[52] A. H. King, Triple lines in materials science and engineering, Scr. Mater. **62**, 889 (2010).
[53] V. D. Nguyen, F. C. Schoemaker, E. M. Blokhuis, and P. Schall, Measurement of the curvature-dependent surface tension in nucleating colloidal liquids, Phys. Rev. Lett. **121**, 246102 (2018).
[54] M. P. Moody and P. Attard, Curvature-dependent surface tension of a growing droplet, Phys. Rev. Lett. **91**, 056104 (2003).
[55] G. Palumbo, S. J. Thorpe, and K. T. Aust, On the contribution of triple junctions to the structure and properties of nanocrystalline materials, Scr. Metall. Mater. **24**, 1347 (1990).
[56] L. Priester, *Grain Boundaries: From Theory to Engineering* (Springer, New York, 2013).
[57] K.-M. Yin, A. H. King, T. E. Hsieh, F.-R. Chen, J. J. Kai, and L. Chang, Segregation of bismuth to triple junctions in copper, Microsc. Microanal. **3**, 417 (1997).
[58] P. Stender, Z. Balogh, and G. Schmitz, Triple junction segregation in nanocrystalline multilayers, Phys. Rev. B **83**, 121407(R) (2011).
[59] Y. Chen and C. A. Schuh, Contribution of triple junctions to the diffusion anomaly in nanocrystalline materials, Scr. Mater. **57**, 253 (2007).
[60] M. Chellali, Z. Balogh, L. Zheng, and G. Schmitz, Triple junction and grain boundary diffusion in the Ni/Cu system, Scr. Mater. **65**, 343 (2011).
[61] G. Gottstein, A. H. King, and L. S. Shvindlerman, The effect of triple-junction drag on grain growth, Acta Mater. **48**, 397 (2000).
[62] A. H. Chokshi, Triple junction limited grain growth in nanomaterials, Scr. Mater. **59**, 726 (2008).
[63] W. C. Carter, M. Baram, M. Drozdov, and W. D. Kaplan, Four questions about triple lines, Scr. Mater. **62**, 894 (2010).
[64] X. Xiao and Z. Wang, Version v1, Zenodo, 10.5281/zenodo.16271853 (2025).